symmetry

IMPACT FACTOR 2.2

CITESCORE 5.4

Article

Geometric Analysis of Black Hole with Primary Scalar Hair

Haotian Liu

Special Issue

Symmetry in Researches of Neutron Stars and Black Holes

Edited by

Dr. Mihaela Parvu and Prof. Dr. Ionel Lazanu

MDPI

https://doi.org/10.3390/sym16111505

symmetry

MDPI

Article

Geometric Analysis of Black Hole with Primary Scalar Hair

Haotian Liu

School of Mathematics, Monash University, Clayton, VIC 3168, Australia; shuaigepangzi@163.com

Abstract: Within the novel context of primary scalar hair black holes, this article explores the fascinating subject of black hole thermal stability. Thermodynamic stability is the main subject of our investigation, which involves measuring the bound points, divergence points, black hole mass, thermal temperature, and specific heat capacity. In addition, we determine the scalar curvatures of thermodynamic geometries like Ruppeiner, Weinhold, Hendi-Panahiyah-Eslam-Momennia, and geometrothermodynamics formulations inside the framework of primary scalar hair black holes and delve into their complexities. Improving our knowledge of fundamental scalar hair black holes, this study sheds light on the intricate thermal geometric properties of these objects.

Keywords: primary scalar hair black hole; thermodynamics; phase transition; thermal geometries; Hawking temperature

Citation: Liu, H. Geometric Analysis of Black Hole with Primary Scalar Hair. *Symmetry* **2024**, *16*, 1505. https://doi.org/10.3390/sym16111505

Academic Editor: Hung T. Diep

Received: 2 October 2024
Revised: 29 October 2024
Accepted: 1 November 2024
Published: 9 November 2024

1. Introduction

Thermodynamics of black holes (BHs) has been an exciting and practical area of study, yielding intriguing findings [1–7]. The relationship between geometrical characteristics like surface gravity and horizon area and thermodynamics values like entropy and temperature is well-established [6,8]. Hawking radiation emission makes BHs thermally unstable, according to semi-classical analysis [9]. Therefore, BHs undergo a full heat loss process in which their temperature rises as their size falls. Among the many thermodynamical aspects of BHs that have been revealed is their heat stability. We can demonstrate the system's integrity following a small change in thermodynamic parameters, since thermal stability is a fundamental thermodynamic property. When investigating a BH's phase structure close to its critical point, several methods are at our disposal [10]. Specific heat is a famous and formal way to analyze the thermal stability of BH. System thermal stability is physically represented by the positive conduct of heat capacity [11,12]. Researching the BH phase transition relies heavily on the heat capacity [12–16]. Heat capacity and divergence of heat capacity are two fundamental kinds of phase transitions. A system's heat capacity is the amount of energy needed to raise or lower its temperature by a specific percentage. A shift in stability is typically indicated by a change in the black hole's heat capacity. Phase transitions from stable to unstable or unstable to stable phases are usually indicated by a change in the sign of the heat capacity. The negative heat capacity of a Schwarzschild BH, for instance, indicates a thermodynamic instability that causes the black hole to be thermally unstable when subjected to Hawking radiation [5,17]. As the system approaches to a critical point, the heat capacity diverges, which is a common sign of a second-order (continuous) phase transition, in which thermodynamic variables vary gradually. Critical events resembling those observed in fluids and other systems are linked to these locations in black hole thermodynamics. One can study the details about these claims in references [10,18].

In a completely different context, a number of writers have developed a geometrical method for thermodynamics and phase transitions. The differential manifold was first proposed by Hermann [19] as a subspace in equilibrium that is entangled with thermodynamic phase space by a natural contact structure. Here, Weinhold proposed an alternative

geometrical method [20] by posing a thermodynamic equilibrium state metric and employing the conformal mapping mechanism from Riemannian to thermodynamic space, which likewise incorporates the geometry of thermodynamic fluctuation. The positive definite line interval in this geometry is connected to two attractive equilibrium states. If we use the Gaussian approximation, the first one describes the distribution of probabilities for thermodynamic fluctuations. A scalar curvature of the thermodynamic properties resulting from this geometry is a written record of the connection underlying the microscopic statistical basis [21,22]. Therefore, the system's correlation volume and divergence at the critical point are related to the scalar curvature.

As a geometrical tool, thermodynamic scalar curvature elucidates the system's macroscopic structure and establishes a connection to its microscopic structure through the application of Gaussian fluctuation. As discussed in the aforementioned research articles [23,24], thermodynamic scalar curvature provides insight into the character of microscopical interaction. Important insights into phase structure, divergency, and critical phenomena for BHs have been proposed using this geometric framework [25–31]. Additionally, the scalar curvature provides thermal stability to the system [20,32]. A BH thermodynamic system in general relativity is similar to the general thermodynamic system in classical physics. All four of thermodynamics' postulates, including the zero law and three more, form the basis of the research. That BHs can radiate particles close to the event horizon via gravitational interactions was initially hypothesized by Hawking [4]. The physics and thermodynamic systems of several kinds of general relativity BH solutions have been extensively researched because of their importance [4]. According to Hawking and Page [5], the phase transition of Schwarzschild AdS BH is studied. The lack of a core singularity makes regular BHs highly intriguing. References [33,34] discuss research on the phase transitions and thermodynamic properties of these BHs. Some other works on BH thermodynamics are also addressed in the literature [32,35–39]. Weinhold and Ruppeiner geometries reveal features of thermodynamic stability and critical phenomena through metrics based on internal energy and entropy, respectively. The Hendi-Panahiyah-Eslam-Momennia (HPEM) approach extends these analyses to more complex BH models, while geometrothermodynamics (GTD) provides a unified framework that captures the full thermodynamic behavior. Utilizing these methods allows for a comprehensive analysis of BH thermodynamics, particularly in understanding phase transitions, stability, and complex behavior in advanced BH models [40–43].

Because of the potential impact of scalar fields produced by BH, the BH with primary scalar hair configuration must be considered in discussions of thermodynamics and optical characteristics. We probe the effects of scalar fields on optical traits by studying the unique geometry of a BH with main scalar hair. A BH can only be completely described by its mass and spin, as stated in the "no-hair" theorem. When things are brought into a BH, no-hair reveals this [44–46]. A fascinating sign that transcends GR would be to look into the hair.

This paper is novel since it investigates thermodynamic geometry in the context of main scalar hair black holes. According to [47], who studied scalar fields, black hole configurations with them offer more flexibility, which could mean stability under some circumstances. Though scalar hair is known to affect a black hole's thermodynamic and physical properties, there are few thermodynamic studies that deal with stability and geometry in scalar hair black holes. Our work contributes to the field by investigating thermal stability using a variety of thermodynamic metrics and geometric methods. In contrast to earlier methods that have relied on individual thermodynamic metrics, our study evaluates stability conditions from several thermodynamic angles by combining different geometric frameworks, such as GTD and the HPEM metric. This work describes the critical behavior caused by scalar hair and compares the behavior of several geometries to reveal possible differences in stability. By demonstrating how scalar hair brings novel features of thermal stability, which may vary substantially from black holes devoid of scalar fields, these results enrich our knowledge of black hole thermodynamics. In addition to shedding new light,

this method points the way toward potential future research directions in the field of black hole thermodynamics.

Following this strategy, we continue our investigation throughout the article. We cover the primary scalar hair BH model's fundamental formalism in Section 2. The topic of thermal stability and phase transition of solutions through heat capacity is covered in Section 3. The geometry of thermodynamics is covered in Section 4, while the outcomes and a summary of our research are found in Section 5.

2. A Short Summary of Primary Scalar Hair Black Hole

The geometry of the primary scalar hair BH is examined in this section. The case study beyond the Horndeski theories is used to create primary scalar hair BH physics [44,48]. Under the condition $\phi \longrightarrow -\phi$, parity symmetry is established, and under the condition $\phi \longrightarrow \phi+$, shift symmetry is provided. G_2, G_4, and F_4 are the three parameterised functions of the scalar-field kinetic term $X = \frac{-1}{2}\partial_\mu\phi\partial^\mu\phi$. The course of action is as follows:

$$S[g_{\mu\nu},\phi] = \frac{1}{2\kappa}\int d^4x\sqrt{-g}\Big(G_2(X) - \phi_{\mu\nu}\phi^{\mu\nu} + G_4(X)R + G_4(X)[(\Box\phi)^2] + F_4(X)\epsilon^{\mu\nu\rho\sigma}\epsilon_\sigma^{\alpha\beta\gamma}\phi_\mu\phi_\alpha\phi_{\nu\beta}\phi_{\rho\gamma}\Big). \tag{1}$$

As the Horndeski functionals are provided by the below equation, the under consideration theory is parameterized by the two coupling constants λ and η, which have dimensions $(length)^4$ and $(length)$, respectively:

$$G_2 = \frac{-8\eta}{3\lambda}X^2,\ G_4 = 1 - \frac{4\eta}{3}X^2,\ F_4 = \eta. \tag{2}$$

This theory is invariant under $\lambda \longrightarrow -\lambda$; therefore, for convenience of notation, λ will always have a positive sign. There is no restriction on the sign of η. The theory admits a homogeneous solution with two integration constants, M and q, where q is not referred to as a primary hair since it does not appear in the metric and does not give rise to any additional charge [46]. The metric function $f(r)$ then appears as:

$$f(r) = 1 - \frac{2M}{r} + \eta q^4\Big(\frac{\pi/2 - \arctan(r/\lambda)}{r/\lambda} + \frac{1}{1+(r/\lambda)^2}\Big), \tag{3}$$

However, the scalar field is stated as:

$$\phi(t,r) = qt + \psi(r)\ ,\ (\psi'(r))^2 = \frac{q^2}{f^2(r)}\left[1 - \frac{f(r)}{1+(r/\lambda)^2}\right], \tag{4}$$

where prime states the derivative related to r in the above equation. The kinetic term linked to the scalar field appears in the following form:

$$X = \frac{q^2/2}{1+(r/\lambda)^2}. \tag{5}$$

The charge q and principal scalar hair, in contrast to stealth solutions, have a significant impact on the metric by modifying it from its GR from M, one of the two autonomous integration constants in the solution that signifies the Arnowitt-Deser-Misner (ADM) mass [45]. Scalar hair vanishes at $q = 0$, resulting in a well-known Schwarschild solution [48]. Spacetime flatness is achieved when q and M disappear. The fundamental scalar hair BH in its spherically symmetric static form is this [46]:

$$ds^2 = -f(r)dt^2 + \frac{dr^2}{f(r)} + r^2(d\theta^2 + \sin^2\theta d\phi^2), \tag{6}$$

Here, the metric function $f(r)$ is represented as:

$$f(r) = 1 - \frac{2M}{r} + \frac{2\lambda^2(\eta q^4)}{r^2} + O\left(\frac{1}{r^4}\right). \tag{7}$$

The above lapse function is just like the Reissner-Nordstrom solution with ADM mass M and main scalar hair q, which scales like electromagnetic charge.

The geometric mass of BH can be found by setting $f(r) = 0$ [40,41]:

$$M = \frac{\eta\lambda^2 q^2 + \eta q^2 r_0^2 + r_0^2}{2r_0}. \tag{8}$$

The entropy can be changed by the introduction of components depending on the strength and dispersion of the scalar field when scalar hair is present, but the BH's mass, charge, and angular momentum remain unchanged. Consequently, the scalar field's properties determine the Bekenstein entropy, which implies that identical BHs can have varying entropies due to variations in the distribution and strength of scalar hair. We are here using the Bekenstein entropy instead of the corrected entropy acting as the thermodynamic quantity: In four-dimensional spacetime, the Einstein-Hilbert action is written as [5]:

$$S_{EH} = \frac{1}{16\pi G}\int d^4x\sqrt{-g}R. \tag{9}$$

with R being the Ricci scalar, g being the metric's determinant, and G being Newton's gravitational constant. If we want to calculate the BH thermodynamics in Euclidean spacetime (imaginary time $\tau = it$), we need to switch to the Euclidean action. Hence, the I_E-function of geometry is:

$$I_E = \frac{1}{16\pi G}\int d^4x\sqrt{g}R, \tag{10}$$

where g and R are currently located in spacetime according to Euclidean geometry. In order to prevent a conical singularity at the horizon, the temperature and the Euclidean time coordinate τ of a BH must be periodic. At $\beta = \frac{1}{T}$, the inverse temperature of the BH is defined by this periodicity. The fourth step is contribution to the horizon and on-shell Euclidean action. The primary factor impacting the evaluation of I_E on the BH solution (on-shell) is a horizon surface term. The action becomes proportional to the horizon area A for a BH [5]:

$$I_E = \frac{A}{4G}. \tag{11}$$

Linking the action of Euclidean space to entropy, a system's entropy S in thermal equilibrium is connected to the Euclidean action according to thermodynamics:

$$S = \beta E - I_E. \tag{12}$$

To calculate the Bekenstein-Hawking entropy for a BH in thermal equilibrium, we use the energy contribution βE and the gravitational action contribution $I_E = \frac{A}{4G}$. The entropy is directly provided by the gravitational action I_E; therefore, we obtain:

$$S = \frac{A}{4G}. \tag{13}$$

If a BH has main scalar hair, then the entropy is not directly proportional to the domain area. Alternatively, the scalar field can influence the BH's entropy calculation by changing its surrounding geometry. In certain altered theories, like scalar-tensor or Horndeski gravity, the entropy-area relationship incorporates contributions from the scalar field. To account for the effect of scalar hair on the thermodynamics of the BH, this can involve adding or modifying variables. The Bekenstein-Hawking entropy equation $S = \frac{kc^3 A}{4G\hbar}$ could need to be tweaked because of the scalar field's interaction with spacetime geometry and the Bekenstein-Hawking haircut. Here is one way to express the BH entropy [5]:

$$S = \pi r_0^2. \tag{14}$$

Here is the first law of thermodynamics [42,43]:

$$dM = TdS. \tag{15}$$

Thermodynamic temperature from first law of thermodynamics is given by:

$$T = \frac{r_0^2(\eta q^2 + 1) - \eta\lambda^2 q^2}{4\pi(r_0^2)^{3/2}}. \tag{16}$$

The thermal temperature of the BH is used to categorize the physical and non-physical solutions to the BH. The non-physical solutions are represented by the region where $T < 0$, whereas the physical solutions are presented by $T > 0$ [49,50]. The temperature along the event horizon for different parameter values of $q,\ \eta,\ \lambda$ is shown in Figure 1, illustrating the direct correlation between these parameters and the thermal behavior of the BH. Reduced thermal temperature is the direct result of raising $q,\ \eta,\ \lambda$. This is because, after a short distance, the thermal temperature becomes positive around the radius of the horizon. These findings based on positive temperature show that our calculated results depict that the BH system is physically and thermally stable.

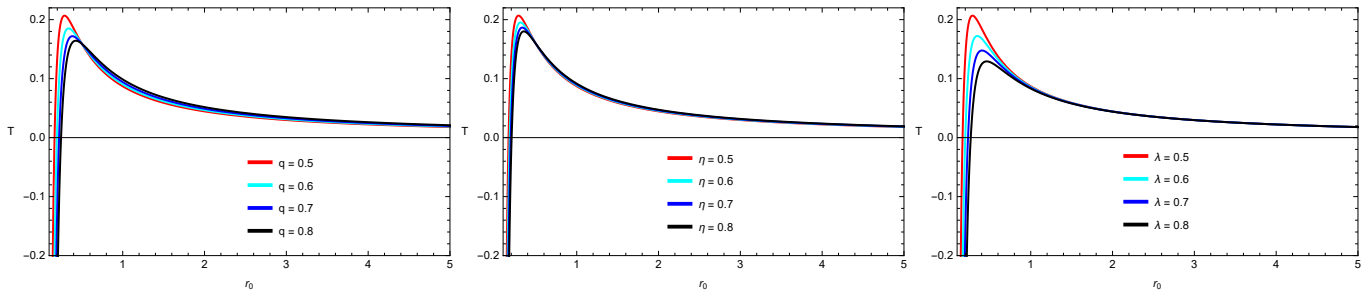

Figure 1. The three plots show the variation of thermodynamic parameter T against horizon radius r_0 under different conditions. **Left panel**: different values of q with fixed $\eta = 0.5,\ \lambda = 0.5$. **Middle panel**: different values of η with fixed $\lambda = 0.5,\ q = 0.5$ **Right panel**: different values of λ with fixed $\eta = 0.5,\ q = 0.5$.

3. Thermal Stability of Solution

The intriguing subject of BH's thermal stability can be uncovered by studying the positive and negative behavior of the specific heat capacity C as it fluctuates. The BH is in a stable area when C is positive, while an unstable condition is predicted by negative values. We can learn a lot about how to understand phase transitions by looking at the disappearance of heat capacity [51–55]. These geometric methods have a general criterion for thermal stability is the positive definiteness of the thermodynamic metric, which is discussed by the eigenvalues of the Hessian matrix directly linked with the thermodynamic potential (internal energy and Bekenstein-Hawking entropy). If all eigenvalues are positive, the system is thermodynamically stable. Conversely, the presence of negative eigenvalues or negative curvature, particularly in GTD, indicates thermodynamic instability or the occurrence of a phase transition. The heat capacity estimate for BH with primary scalar hair looks like this:

$$C = -\frac{2\pi r_0^2(r_0^2(\eta q^2 + 1) - \eta\lambda^2 q^2)}{r_0^2(\eta q^2 + 1) - 3\eta\lambda^2 q^2}. \tag{17}$$

For different values of $q,\ \eta,\ \lambda$, the transitional phase of the heat capacity is presented in Figure 2. A root point and a heat capacity divergence are shown on the graph, which represent the physical limits and critical points of phase transition, respectively. At the outset, heat capacity points to a stable area for small event horizon r_0 values, but it changes to a globally unstable area and stays unstable after that. It should be noted that the parameters $q,\ \eta,\ \lambda$ determine the key points for phase transition, which might vary depending on values. In light of the foregoing, it may be useful to examine where the

concept of heat capacity came from and how it has evolved. We find the bound points, which are the roots of the heat capacity, as shown below [56]:

$$r_{0\{\pm\}}, B.P = \pm\frac{\sqrt{\eta}\lambda q}{\sqrt{\eta q^2+1}}, \tag{18}$$

and divergence points are:

$$r_{0\{\pm\}}, D.P = \pm\frac{\sqrt{3}\sqrt{\eta}\lambda q}{\sqrt{\eta q^2+1}}. \tag{19}$$

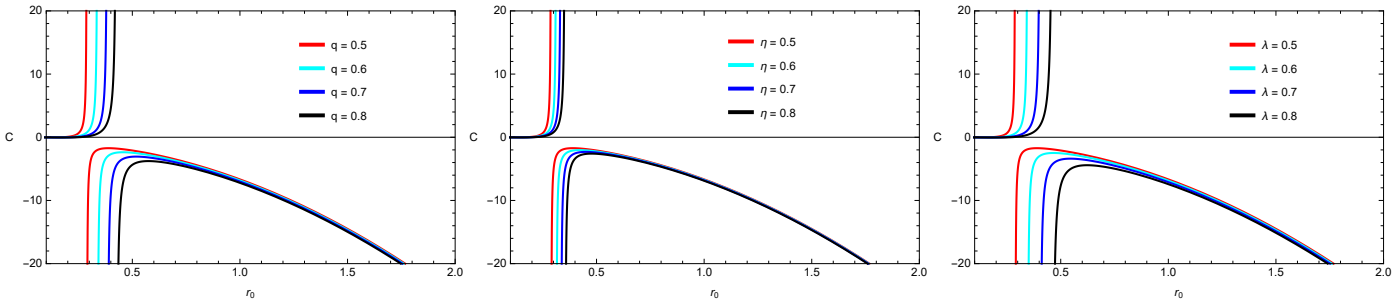

Figure 2. The three plots show the variation of heat capacity C against horizon radius r_0 under different conditions. **Left panel**: different values of q with fixed $\eta = 0.5$, $\lambda = 0.5$. **Middle panel**: different values of η with fixed $\lambda = 0.5$, $q = 0.5$ **Right panel**: different values of λ with fixed $\eta = 0.5$, $q = 0.5$.

The bound points are denoted by the subscript B.P, whereas the divergence points are shown by the subscript D.P. There are two potential roots of the heat capacity. They need to meet the criterion $\lambda \geq 0$ in order to be real roots. B.P and D.P as functions of q, η, λ that decrease and increase depending on the values of parameters. The positive and negative bound points and divergence points can be seen in Figures 3 and 4.

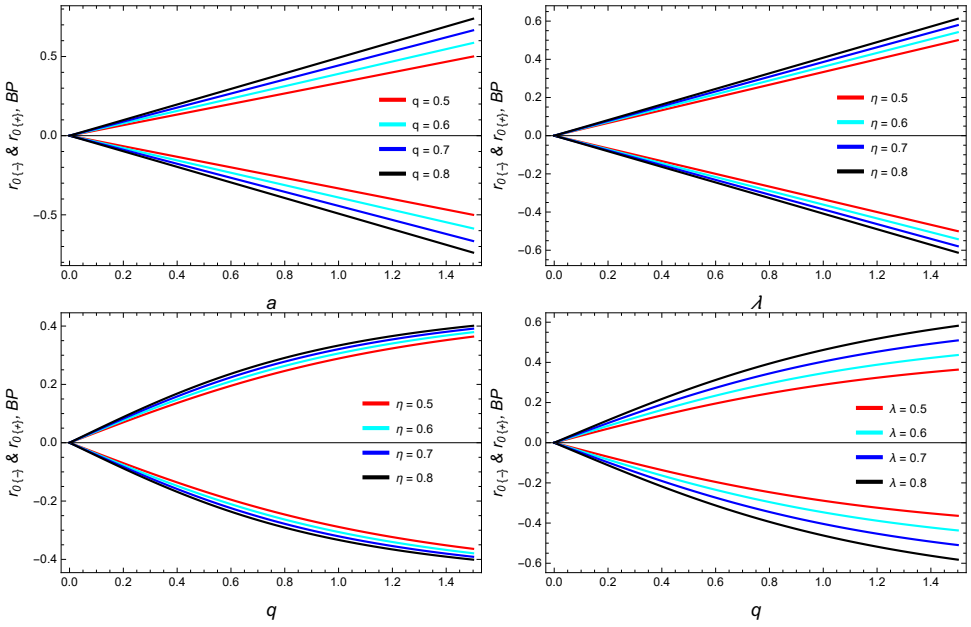

Figure 3. *Cont.*

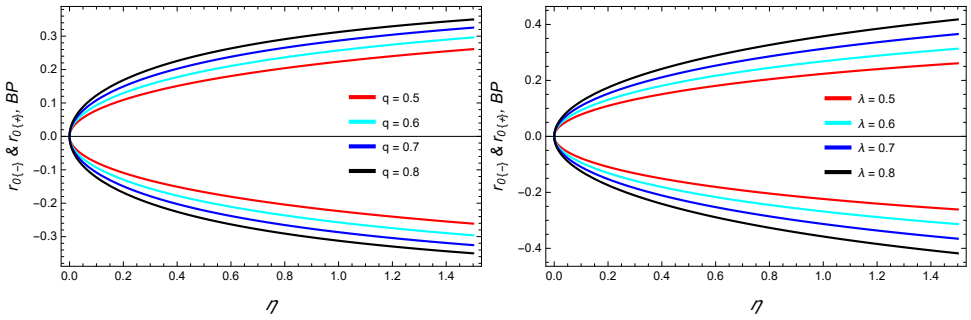

Figure 3. Bound points $r_{0\{\pm\}}$, B.P along horizon radius r_0. Here, we fix $\eta = 0.5$, $\lambda = 0.5$, $q = 0.5$ (**first-row left** graph along a for different values of q given in legend, **first-row right** graph along λ for different values of η given in legend, **second row** both graph along q **left** different for values of η and **right** for different values of λ given in legend, **third row** both graph along η **left** for different values of q and **right** for different values of λ given in legend).

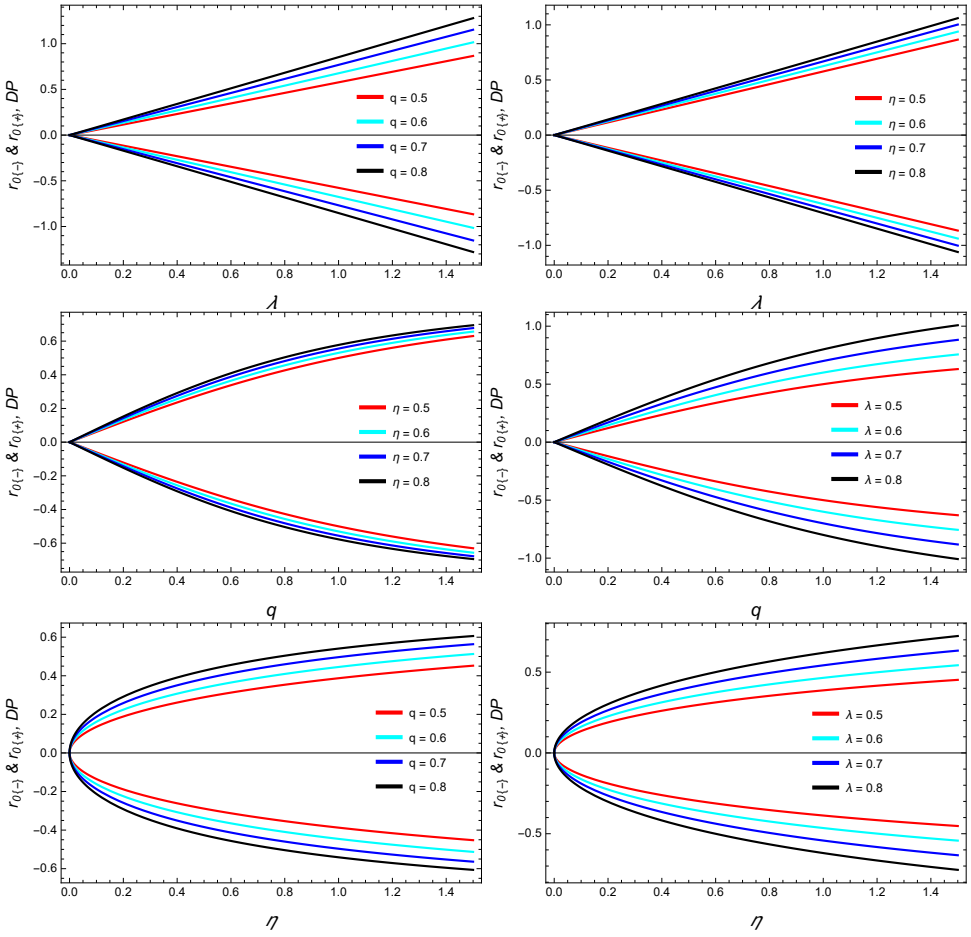

Figure 4. Divergence points $r_{0\{\pm\}}$, D.P along horizon radius r_0. Here, we fix $\eta = 0.5$, $\lambda = 0.5$, $q = 0.5$ (**first row** both graph along λ **left** for different values of q right for different values of η given in legend, **second row** both graph along q **left** different for values of η and **right** for different values of λ given in legend, **third row** both graph along η **left** for different values of q and **right** for different values of λ given in legend).

4. Thermodynamic Geometries

Thermodynamic studies of BHs have shown that, in many cases, the exact causes of the system's mass, temperature, and heat capacity anomalies are not known. Many efforts have been undertaken in the last few decades to integrate various geometric ideas into standard thermodynamics. The thermodynamic phase space is best understood as

a differential manifold with an intrinsic contact structure, where a separate subspace of equilibrium states is present. According to many observations, the geometric framework appears to quantify the system's underlying statistical mechanics. In systems without statistical mechanical interactions (e.g., ideal gas), the Ruppeiner geometry is flat, and a non-zero Ruppeiner curvature is suggestive of a phase transition [57]. Numerous studies support these conclusions [58,59]. Furthermore, the Ruppeiner metric is connected to the Weinhold metric, which defines the Hessian of energy (mass) [32,60]. Here, we will explore the intriguing realm of thermodynamical geometries obtained for primary scalar hair BHs by Weinhold and Ruppeiner [49]. We still do not have a full picture of the microstructure of BHs, even though we have studied their thermodynamics a lot. The good news is that geometric analysis of thermodynamic systems provides a way to investigate the microstructure of BHs [57].

The reason why this invariant approach should be preserved is that the entropy difference and the probability of fluctuation between two states should be independent of the system's coordinates. We introduce a new and valuable component for our discussion, the thermodynamic length, because the portion of $g_{\mu\nu}\Delta\mathcal{E}^{\mu}\Delta\mathcal{E}^{\nu}$ resembles a Riemannian metric representing a distance between thermodynamic states [61]:

$$\Delta\ell^2 \equiv g_{\mu\nu}\Delta\mathcal{E}^{\mu}\Delta\mathcal{E}^{\nu}, \tag{20}$$

that is definitely positive. Riemannian metrics in the space of thermodynamic states are well-defined, and the relation above is no exception. Given this space and two thermodynamic states, the physical meaning of the distance between them is crystal clear: it is a measure of probability in thermodynamics. Two states are thought to be closer together if there is a higher possibility of a fluctuation occurring between them. As an aside, in general relativity (GR), the square of the thermodynamic length is usually measured in meters squared, although in Riemannian geometry, the square of the length is inversely related to volume.

The Figures 3 and 4 are different shape of the metric can be investigated in other coordinate systems, but the value of $\Delta\ell^2$ must remain constant regardless of these systems. A number of thermodynamic coordinate systems have the form of the Ruppeiner metric, which will be determined with this in mind: $\left(u, \mathcal{E}^i\right)$, As already explained, working with systems where the coordinates are extended parameters, denoted as $\left(u, \mathcal{E}^1, \mathcal{E}^2, \ldots, \mathcal{E}^r\right)^1$, results in the following [32,61]:

$$g^R_{\mu\nu} = -\frac{1}{k_B}\frac{\partial^2 s}{\partial\mathcal{E}^{\mu}\partial,\mathcal{E}^{\nu}}, \tag{21}$$

This is the Hessian matrix representing the thermodynamic entropy (14). Additionally, the thermodynamic stability requires that $g^R_{\mu\nu}$ be positively charged. The extensive and intense characteristics are used to define an alternative coordinate system. For this situation, we obtain by using the aforementioned equations and the transfer function $\Delta\mathcal{E}^{\mu} = \frac{\partial\mathcal{E}^{\mu}}{\partial x^{\alpha}}\Delta x^{\alpha}$:

$$\Delta\ell^2 = -\frac{1}{k_B}\Delta\mathcal{I}^{\mu}\Delta\mathcal{E}_{\mu}. \tag{22}$$

Furthermore, in order to fully express the metric using the intense parameters, we employ:

$$\Delta\mathcal{E}^{\mu} = \frac{\partial\mathcal{E}^{\mu}}{\partial\mathcal{I}^{\alpha}}\Delta\mathcal{I}^{\alpha}. \tag{23}$$

and plugging this into Equation (22) produces:

$$\Delta\ell^2 = \frac{1}{k_B}\frac{\partial^2\phi}{\partial\mathcal{I}^{\mu}\partial\mathcal{I}^{\nu}}\Delta\mathcal{I}^{\mu}\Delta\mathcal{I}^{\nu}, \tag{24}$$

where ϕ is the Legendre transformation of the entropy with respect to all extensive system parameters (except volume) and is expressed as [61]:

$$\phi\left(\mathcal{I}^0, \mathcal{I}^1, \ldots, \mathcal{I}^r\right) = s - \mathcal{I}^\mu \mathcal{E}_\mu, \tag{25}$$

The intense parameters, while working in the entropy representation, can be determined in the following way:

$$\left\{\mathcal{I}^0, \mathcal{I}^i\right\} = \left\{\frac{1}{T}, -\frac{\mu^i}{T}\right\}, \tag{26}$$

for each component of the fluid, where μ^i represents its chemical potential. By plugging the given relation into Equation (22), we may obtain:

$$\begin{aligned}
\Delta\mathcal{E}^0 &= \Delta u = T\Delta s + \sum_{i=1}^{r} \mu^i \Delta\mathcal{E}^i, \\
\Delta\mathcal{I}^0 &= -\frac{1}{T^2}\Delta T, \\
\Delta\mathcal{I}^i &= \frac{\mu^i}{T^2}\Delta T - \frac{1}{T}\Delta\mu^i, \quad 1 \le i \le r,
\end{aligned}$$

this becomes as

$$\Delta\ell^2 = \frac{1}{k_B T}\Delta T\Delta s + \frac{1}{k_B T}\sum_{i=1}^{r} \Delta\mu^i \Delta\mathcal{E}^i. \tag{27}$$

In the coordinate system $\left(T, \mathcal{E}^1, \mathcal{E}^2, \ldots, \mathcal{E}^r\right)$, we can determine the shape of the metric. In order to do this, we employ the subsequent relation:

$$\begin{aligned}
\Delta s &= \frac{\partial s}{\partial T}\Delta T + \sum_{i=1}^{r} \frac{\partial s}{\partial \mathcal{E}^i}\Delta\mathcal{E}^i, \\
\Delta\mu^i &= \frac{\partial \mu^i}{\partial T}\Delta T + \sum_{i=1}^{r} \frac{\partial \mu^i}{\partial \mathcal{E}^i}\Delta\mathcal{E}^i,
\end{aligned}$$

as well as the Maxwell relation

$$\frac{\partial s}{\partial \rho^i} = -\frac{\partial \mu^i}{\partial T}, \tag{28}$$

and substituting Equation (28) into Equation (27), we obtain

$$\Delta\ell^2 = \frac{1}{k_B T}\frac{\partial s}{\partial T}(\Delta T)^2 + \frac{1}{k_B T}\sum_{i,j=1}^{r} \frac{\partial \mu^i}{\partial \mathcal{E}^j}\Delta\mathcal{E}^i\Delta\mathcal{E}^j. \tag{29}$$

First, we will look at the basic features of theories of thermodynamic geometry. A metric space is important to the equilibrium state space of a thermodynamic system, and this idea bridges the gap between thermodynamics and statistical mechanics. The Weinhold geometry, as mentioned in [32], can be expressed in terms of mass M:

$$g_{ij}{}^{W} = \partial_i \partial_j M(S,\ \eta,\ \lambda,\ q). \tag{30}$$

The metric for primary scalar hair BH can be stated as:

$$ds_W^2 = M_{SS}dS^2 + M_{qq}dq^2 + 2M_{qs}dqdS, \tag{31}$$

whose matrix form is given by:

$$\begin{pmatrix} M_{SS} & M_{Sq} \\ M_{qS} & M_{qq} \end{pmatrix}. \tag{32}$$

If we have the matrix and the equations, we can calculate the curvature scalar of the Weinhold metric $R(wein)$. To determine the covariant metric tensor, Christoffel symbols,

Riemann tensor, and Ricci tensor, we employed the Hessian matrix MAPLE program. The non-zero components of the Ricci tensor are:

$$R_{11} = -\frac{1}{8}\frac{\left(-q^2\eta S + 3q^2\eta\pi\lambda^2 - S\right)\left(-S + 3\pi\lambda^2\right)\left(S + \pi\lambda^2\right)}{S(-3q^2\eta S^2 + 6q^2\eta S\pi\lambda^2 + q^2\eta\pi^2\lambda^4 - S^2 - S\pi\lambda^2)^2},$$
$$R_{12} = \frac{1}{2}\frac{q\left(-S + \pi\lambda^2\right)\left(-S + 3\pi\lambda^2\right)\eta\left(S + \pi\lambda^2\right)}{(-3q^2\eta S^2 + 6q^2\eta S\pi\lambda^2 + q^2\eta\pi^2\lambda^4 - S^2 - s\pi\lambda^2)^2},$$
$$R_{22} = -\frac{\left(S + \pi\lambda^2\right)^2 S\left(-S + 3\pi\lambda^2\right)\eta}{(-3q^2\eta S^2 + 6q^2\eta S\pi\lambda^2 + q^2\eta\pi^2\lambda^4 - S^2 - S\pi\lambda^2)^2}.$$

The Ruppeiner has been computed by combining the Ricci scalar with temperature. This scalar's mathematical expression looks like this:

$$R(wein) = \frac{2\sqrt{\pi}\left(\pi\lambda^2 + S\right)S^{3/2}\left(S - 3\pi\lambda^2\right)}{\left(\pi^2\eta\lambda^4q^2 - 3\eta q^2S^2 + 6\pi\eta\lambda^2q^2S - S^2 - \pi\lambda^2S\right)^2}. \tag{33}$$

Upon careful examination of Figure 5, an interesting finding becomes apparent: there is no singularity seen in the curvature scalar of the Weinhold geometry of the fundamental scalar BH. This suggests that the Weinhold metric has interesting information about the phase transition (no change between the negative and positive areas), and that its high negative value would lead to a strong attractive interaction in the BH microstructure [62]. The next analysis will include computing the conformal to the Weinhold as well as Ruppeiner geometry. According to [63], the Ruppeiner metric for a thermodynamic system is as follows:

$$ds^2_{RUP} = \frac{ds^2_W}{T}. \tag{34}$$

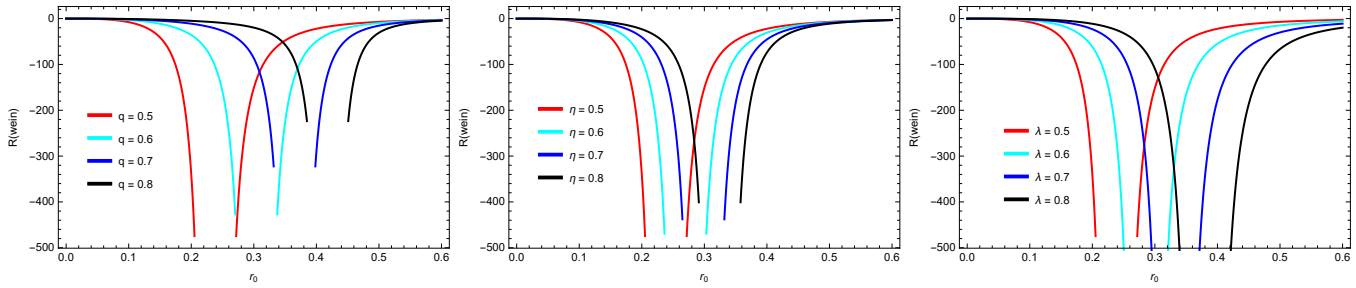

Figure 5. Weinhold geometry R(wein) along horizon radius r_0. Here, we fix $\eta = 0.5$, $\lambda = 0.5$, $q = 0.5$ (**left panel** for different values of q, **middle panel** for different values of η, and **right panel** for different values of λ given in legend).

The expression for Ruppeiner geometry is stated as below:

$$R(RUP) = \frac{8\pi\, S^3\left(S - 3\,\pi\,\lambda^2\right)\left(S + \pi\,\lambda^2\right)}{(q^2(S - \pi\,\lambda^2)\eta + S)(-3\,q^2\eta\,S^2 + 6\,q^2\eta\,S\pi\,\lambda^2 + q^2\eta\,\pi^2\lambda^4 - S^2 - S\pi\,\lambda^2)^2}. \tag{35}$$

The curvature scalar of Ruppeiner geometry is not singular for various q, η, λ values, as can be seen in Figure 6. Moreover, it is positive for the short-range of r_0, and afterward, it is negative. This is the motivation of the present study. The HPEM geometry follows as:

$$ds^2 = \frac{SM_S}{\left(\frac{\partial^2 M}{\partial q^2}\right)^3}(-M_{SS}dS^2 + M_{qq}dq^2). \tag{36}$$

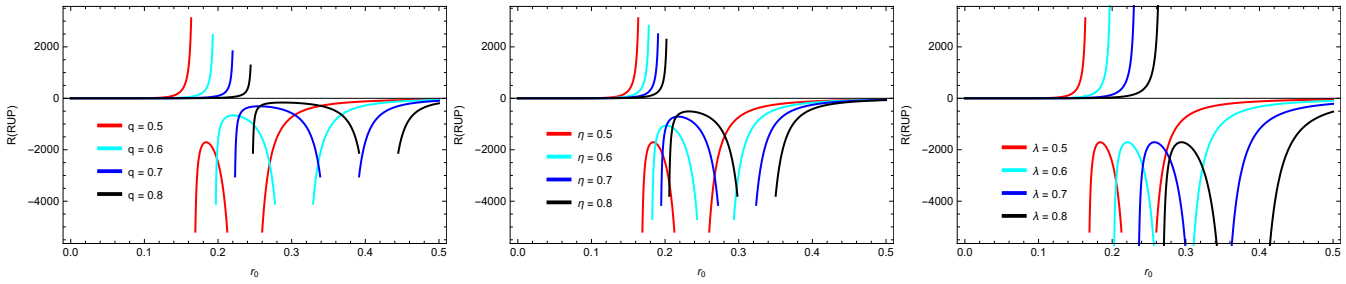

Figure 6. Ruppenier geometry $R(RUP)$ along horizon radius r_0. Here, we fix $\eta = 0.5$, $\lambda = 0.5$, $q = 0.5$ (**left panel** for different values of q, **middle panel** for different values of η, and **right panel** for different values of λ given in legends).

The mathematical expression for the HPEM geometry scalar is calculated as:

$$R(HPEM) = \frac{S^{5/2}\left(S-3\pi\lambda^2\right)\pi^{3/2}\left(S\left(\eta q^2+1\right)-\pi\eta\lambda^2q^2\right)}{2\eta^3(\pi\lambda^2+S)^4\left(S\left(\eta q^2+1\right)-3\pi\eta\lambda^2q^2\right)^2}.$$

By examining the singularity-free behavior of the HPEM curvature scalar, one can derive valuable insights from Figure 7. Since the zero point of the HPEM metric's divergence of scalar curvature is near the heat capacity, we can derive useful information from this formalism. In Figure 8, we examine the scalar behavior of GTD curvature. In such instances, we found that the GTD curvature and the zero point of heat capacity are synchronous. Here, the GTD geometry provides all the physical details of this structure. The GTD metric can be expressed as:

$$ds^2 = (SM_{SS} + qM_{qq})\begin{pmatrix} -M_{SS} & 0 \\ 0 & m_{qq} \end{pmatrix}. \tag{37}$$

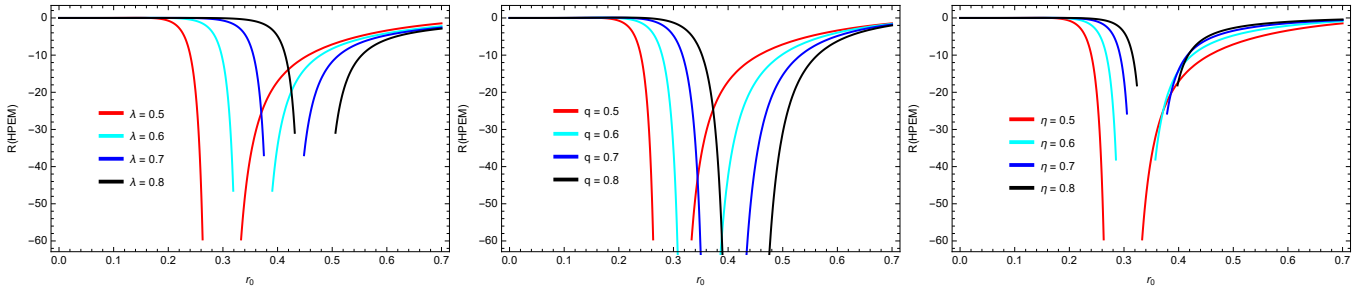

Figure 7. HPEM geometry $R(HPEM)$ along horizon radius r_0. Here, we fix $\eta = 0.5$, $\lambda = 0.5$, $q = 0.5$ (**left panel** for different values of λ, **middle panel** for different values of q, and **right panel** for different values of η given in legends).

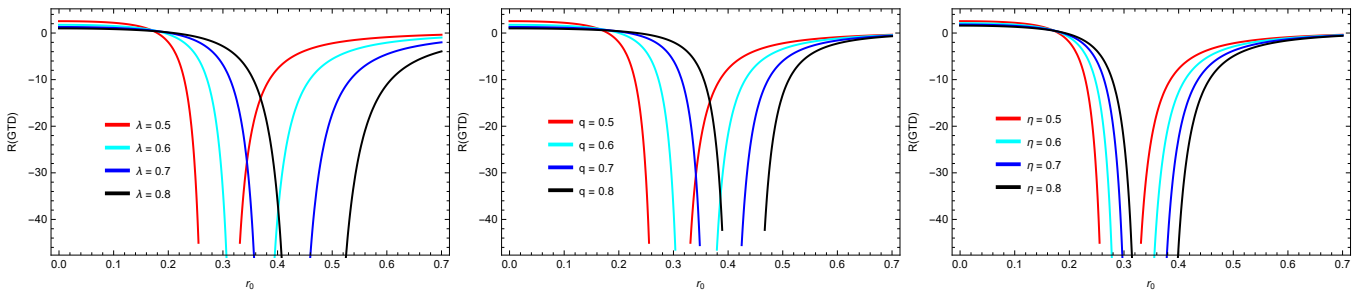

Figure 8. GTD geometry $R(GTD)$ along horizon radius r_0. Here, we fix $\eta = 0.5$, $\lambda = 0.5$, $q = 0.5$ (**left panel** for different values of λ, **middle panel** for different values of q, and **right panel** for different values of η given in legends).

From the above expression, one can obtain:

$$R(GTD) = \frac{(S-3\pi\lambda^2)\left(-3\pi\eta\lambda^2q^2+8\eta qS^2+S\left(\eta q\left(8\pi\lambda^2+q\right)+1\right)\right)}{4(\pi\lambda^2+S)(S(\eta q^2+1)-3\pi\eta\lambda^2q^2)^2}.$$

Figures 9 and 10 illustrate how effectively the Weinhold and Ruppeiner approaches work with heat capacity zeros. The resulting curvature scalar of the Ruppiner and Weinhold metrics is shown in terms of the horizon radius r_h in order to investigate the thermodynamic phase transition. There is a physical limitation point and one zero point in the heat capacity at $r_h = 1.651$. Figure 11 shows that the zero points of heat capacity coincide with the divergence of the scalar curvature of the HPEM metric. Consequently, the HPEM formalism can yield some valuable insights. Furthermore, learning about the scalar curvature of thermodynamic geometry is essential since HPEM metrics can show how a BH's principal scalar hair diverges. The divergences of the BH with primary scalar hair coincide with the GTD approach in Figure 12. Here, we highlight the impact of various spacetime parameter values on the BH's stability requirements. The figure shows that similar to the BH in the preceding section, this likewise exhibits phase change. The zero point of heat capacity coincides with the GTD scalar when q is set. Therefore, it is possible to glean some relevant data from this situation.

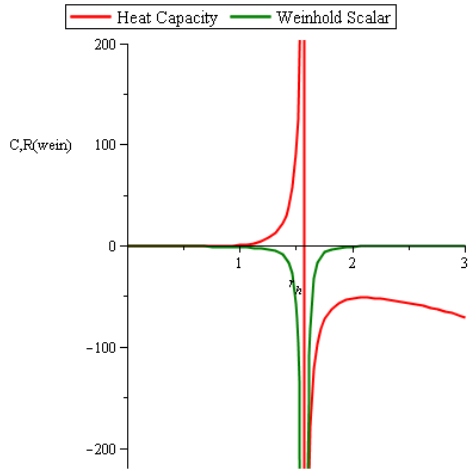

Figure 9. Plot of Weinhold curvature scalar $R^{(Wein)}$ with heat capacity of fixed values $q = 0.5$, $\eta = 2.3$ and $\lambda = 1.5$.

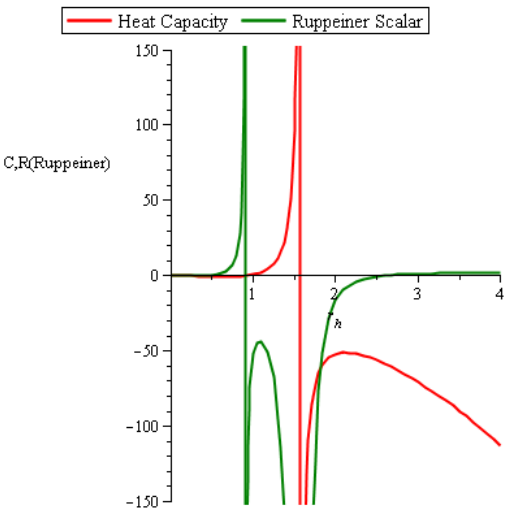

Figure 10. Plot of Ruppeiner curvature scalar $R^{(Rup)}$ with heat capacity of fixed values $q = 0.5$, $\eta = 1.5$ and $\lambda = 1.5$.

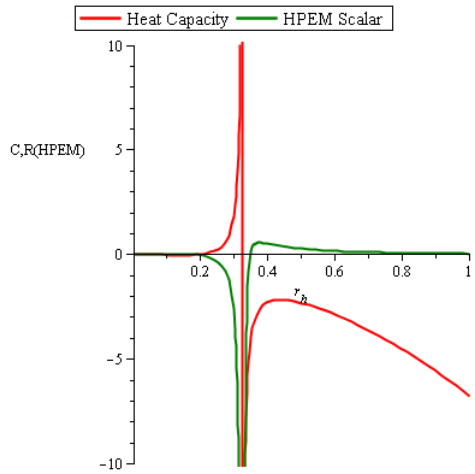

Figure 11. Plot of HPEM curvature scalar $R^{(HPEM)}$ with heat capacity of fixed values $q = 2.5$, $\eta = 1.2$ and $\lambda = 0.5$.

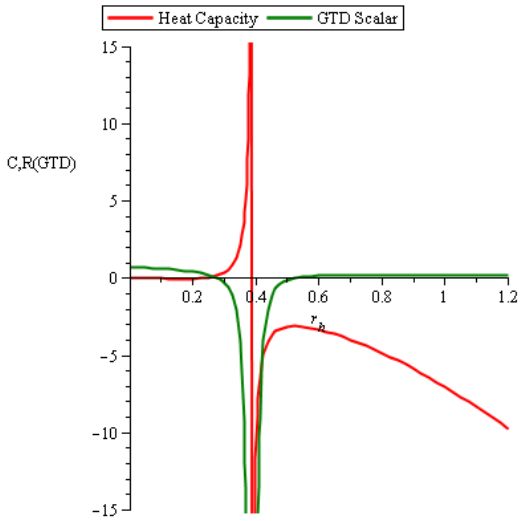

Figure 12. Plot of GTD curvature scalar $R^{(GTD)}$ with heat capacity of fixed values $q = 2.5$, $\eta = 0.2$ and $\lambda = 0.3$.

5. Results and Conclusions

In this article, we examine the ansatz of a primary scalar hair BH and examine its complete properties through graphical analysis. These characteristics include: geometric mass; geometric interpretations of BHs in relation to the Weinhold, Ruppeiner, HPEM, and GTD formalisms; phase transition via heat capacity; bond points; and divergence points. The findings demonstrate the physical existence and thermodynamic stability of BHs. It should be noted that these findings differ sufficiently from relevant previous work in terms of phase transition points and stable-unstable zones, and are more precise. We arrive at the following results summary:

The BH solution is stable since the thermal temperature is behaving positively. There is an inverse relationship between the parameters q, η, λ and thermal temperature in terms of behavior. Based on the parameters of q, η, λ, the heat capacity behavior in our example shows that the BH model is thermally stable (positive) with an initially unstable zone (negative). It also sheds light on the crucial sites for phase transition. The geometrical composition of primary scalar hair BH has been determined using the Weinhold and Ruppeiner formalism. It has been found that these geometries do not contain singularities, behave attractively (negatively) in the thermodynamic system, and do not reveal anything

about the phase transition. As a measure of phase transition, zero points of heat capacity correlate with HPEM and GTD scalar curvature divergence.

The Weinhold and Ruppeiner methods reveal the features of thermodynamic stability and critical phenomena through metrics based on internal energy and entropy, respectively. The HPEM approach extends to the analysis of primary scalar hair BH, while GTD provides a unified framework that captures the full thermodynamic behavior. Utilizing these methods allows us to comprehensively analyze the BH stability, particularly in understanding the microstructure of primary scalar hair BH. Moreover, we have compared our results with recent papers [41–43] and find that this approach plays an important role in physics and thermodynamic systems of specific BH solutions in general relativity.

As proposed in [64], future research should broaden the scope of scalar fields' examination in black hole thermodynamics to include non-minimally coupled and time-dependent scalar fields, among others. By extending this model, we can learn more about the effects of different scalar field features on the stability of black hole systems. Theoretical predictions of scalar hair stability could be further empirically supported by comparisons with current observational evidence, especially from the Event Horizon Telescope (EHT). We argue that our results could be more applicable with empirical validation, building on frameworks [65] that link black hole thermodynamic models with EHT observational data. It is possible that, in the future, researchers will broaden their focus to include multi-hair black hole models and more complicated black hole systems to see if the patterns of thermal stability seen in primary scalar hair black holes are applicable to these or other scalar field configurations. By using this route, thermodynamic geometry may be able to describe more phenomena observed in the field of black hole astrophysics.

Funding: This research received no external funding.

Data Availability Statement: Data are contained within the article.

Acknowledgments: I am deeply grateful to Todd Oliynik for his invaluable guidance and insightful contributions, which have significantly enhanced the quality of this manuscript.

Conflicts of Interest: The author declares no conflict of interest.

References

1. Bekenstein, J.D. Black holes and entropy. *Phys. Rev. D* **1973**, *7*, 2333–2346. [CrossRef]
2. Bekenstein, J.D. Generalized second law of thermodynamics in black-hole physics. *Phys. Rev. D* **1974**, *9*, 3292–3300. [CrossRef]
3. Hawking, S.W. Particle creation by black holes. *Commun. Math. Phys.* **1975**, *43*, 199–220. [CrossRef]
4. Hawking, S.W. Black holes and thermodynamics. *Phys. Rev. D* **1976**, *13*, 191–197. [CrossRef]
5. Hawking, S.W.; Page, D.N. Thermodynamics of black holes in anti-de Sitter space. *Commun. Math. Phys.* **1983**, *87*, 577–588. [CrossRef]
6. Bardeen, J.M.; Carter, B.; Hawking, S.W. The four laws of black hole mechanics. *Commun. Math. Phys.* **1973**, *31*, 161–170. [CrossRef]
7. Gibbons, G.W.; Hawking, S.W. Action integrals and partition functions in quantum gravity. *Phys. Rev. D* **1977**, *15*, 2752–2756. [CrossRef]
8. Hawking, S.W. Black hole explosions? *Nature* **1974**, *248*, 30–31. [CrossRef]
9. Wald, R.M. The thermodynamics of black holes. *Living Rev. Relativ.* **2001**, *4*, 6. [CrossRef]
10. Kubiznak, D.; Mann, R.B. P–V criticality of charged AdS black holes. *J. High Energy Phys.* **2012**, *2012*, 33.
11. Padmanabhan, T. Entropy of static spacetimes and microscopic density of states. *Class. Quant. Grav.* **2004**, *21*, 4485. [CrossRef]
12. Myung, Y.S. Thermodynamics of the Schwarzschild-de Sitter black hole: Thermal stability of the Nariai black hole. *Phys. Rev. D* **2008**, *77*, 104007.
13. Davies, P.C.W. Thermodynamic phase transitions of Kerr-Newman black holes in de Sitter space. *Class. Quant. Grav.* **1989**, *6*, 1909. [CrossRef]
14. Surya, S.; Schleich, K.; Witt, D.M. Phase Transitions for Flat Anti–de Sitter Black Holes. *Phys. Rev. Lett.* **2001**, *86*, 5231–5234. [CrossRef]
15. Zou, D.-C.; Zhang, S.-J.; Wang, B. Critical behavior of Born-Infeld AdS black holes in the extended phase space thermodynamics. *Phys. Rev. D* **2014**, *89*, 044002. [CrossRef]
16. Sahay, A.; Sarkar, T.; Sengupta, G. Thermodynamic geometry and phase transitions in Kerr-Newman-AdS black holes. *J. High Energy Phys.* **2010**, *1004*, 118. [CrossRef]

17. Davies, P.C.W. The Physics of Time Asymmetry. *Class. Quantum Gravity* **1977**, *13*, 2105–2111.
18. Chamblin, A.; Emparan, R.; Johnson, C.V.; Myers, R.C. Charged AdS black holes and catastrophic holography. *Phys. Rev. D* **1999**, *60*, 064018. [CrossRef]
19. Hermann, R. *Geometry, Physics, and Systems*; Marcel Dekker, Inc.: New York, NY, USA, 1973.
20. Weinhold, F. Metric geometry of equilibrium thermodynamics. *J. Chem. Phys.* **1975**, *63*, 2479–2483. [CrossRef]
21. Chaturvedi, P.; Das, A.; Sengupta, G. Thermodynamic geometry and phase transitions of dyonic charged AdS black holes. *Eur. Phys. J. C* **2017**, *77*, 110. [CrossRef]
22. Capela, F.; Nardini, G. Hairy black holes in massive gravity: Thermodynamics and phase structure. *Phys. Rev. D* **2012**, *86*, 024030. [CrossRef]
23. Sahay, A.; Sarkar, T.; Sengupta, G. On the thermodynamic geometry and critical phenomena of AdS black holes. *J. High Energy Phys.* **2010**, *2010*, 82. [CrossRef]
24. Mirza, B.; Mohammadzadeh, H. Nonperturbative thermodynamic geometry of anyon gas. *Phys. Rev. E* **2008**, *78*, 021127. [CrossRef] [PubMed]
25. Gunasekaran, S.; Mann, R.B.; Kubiznak, D. Extended phase space thermodynamics for charged and rotating black holes and Born-Infeld vacuum polarization. *J. High Energy Phys.* **2012**, *11*, 110. [CrossRef]
26. Rajagopal, A.; Kubiznak, D.; Mann, R.B. Van der Waals black hole. *Phys. Lett. B* **2014**, *737*, 277–279. [CrossRef]
27. Xu, J.; Cao, L.; Hu, Y. P–V criticality in the extended phase space of black holes in massive gravity. *Phys. Rev. D* **2015**, *91*, 124033. [CrossRef]
28. Hendi, S.H.; Panahiyan, S.; Panah, B.E. P–V criticality and geometrical thermodynamics of black holes with Born–Infeld type nonlinear electrodynamics. *Int. J. Mod. Phys. D* **2016**, *25*, 1650010. [CrossRef]
29. Hendi, S.; Vahidinia, M.H. Extended phase space thermodynamics and P–V criticality of black holes with a nonlinear source. *Phys. Rev. D* **2013**, *88*, 084045. [CrossRef]
30. Mo, J.; Li, G.; Xu, X. Effects of power-law Maxwell field on the critical phenomena of higher dimensional dilaton black holes. *Phys. Rev. D* **2016**, *93*, 084041. [CrossRef]
31. Li, G. Effects of dark energy on P–V criticality of charged AdS black holes. *Phys. Lett. B* **2014**, *735*, 256–260. [CrossRef]
32. Ruppeiner, G. Riemannian geometry in thermodynamic fluctuation theory. *Rev. Mod. Phys.* **1995**, *67*, 605–659. [CrossRef]
33. Chaudhary, S.; Jawad, A.; Yasir, M. Thermodynamic geometry and Joule-Thomson expansion of black holes in modified theories of gravity. *Phys. Rev. D* **2022**, *105*, 024032. [CrossRef]
34. Shahzad, M.U.; Nazir, M.A.; Jawad, A. Consequences of thermal geometries in Brane-World black holes. *Phys. Dark Univ. D* **2021**, *32*, 100828. [CrossRef]
35. Ditta, A.; Tiecheng, X.; Mustafa, G.; Yasir, M.; Atamurotov, F. Thermal stability with emission energy and Joule–Thomson expansion of regular BTZ-like black hole. *Eur. Phys. J. C* **2022**, *82*, 756. [CrossRef]
36. Ditta, A.; Tiecheng, X.; Ali, R.; Mustafa, G.; Mahmood, A. Thermal properties of Simpson–Visser Minkowski core regular black holes solution in Verlinde's emergent gravity. *Phys. Dark Univ. D* **2024**, *43*, 101418. [CrossRef]
37. Ditta, A.; Javed, F.; Mustafa, G.; Maurya, S.K.; Sofuoglu, D.; Atamurotov, F. Thermal analysis of charged Symmergent black hole with logarithmic correction. *Chin. J. Phys.* **2024**, *88*, 287–300. [CrossRef]
38. Ditta, A.; Mumtaz, S.; Mustafa, G.; Maurya, S.K.; Atamurotov, F.; Mahmood, A. Thermal analysis of gravitational decoupling black hole solution. *J. High Energy Astro. Phys.* **2024**, *42*, 146–155. [CrossRef]
39. Ditta, A.; Bouzenada, A.; Mustafa, G.; Alanazi, Y.M.; Mushtaq, F. Particle motion, shadows and thermodynamics of regular black hole in pure gravity. *Phys. Dark Univ. D* **2024**, *46*, 101573. [CrossRef]
40. Dolan, B.P. Pressure and volume in the first law of black hole thermodynamics. *Class. Quant. Grav.* **2011**, *28*, 235017. [CrossRef]
41. Feng, H.; Huang, Y.; Hong, W.; Tao, J. Charged torus-like black holes as heat engines. *Commun. Theor. Phys.* **2021**, *73*, 045403. [CrossRef]
42. Sakalli, I.; Ovgun, A. Hawking radiation and deflection of light from Rindler modified Schwarzschild black hole. *Europhys. Lett.* **2017**, *118*, 60006. [CrossRef]
43. Anabalón, A.; Appels, M.; Gregory, R.; Kubizňák, D.; Mann, R.B.; Ovgün, A. Holographic thermodynamics of accelerating black holes. *Phys. Rev. D* **2018**, *98*, 104038. [CrossRef]
44. Gleyzes, J.; Langlois, D.; Piazza, F.; Vernizzi, F. Healthy theories beyond Horndeski. *arXiv* **2014**, arXiv:1404.6495.
45. Arnowitt, R.; Deser, S.; Misner, C.W. Coordinate invariance and energy expressions in general relativity. *Phys. Rev.* **1961**, *122*, 997–1006.
46. Bakopoulos, A.; Charmousis, C.; Kanti, P.; Lecoeur, N.; Nakas, T. Black holes with primary scalar hair. *Phys. Rev. D* **2024**, *109*, 024032. [CrossRef]
47. Herdeiro, C.A.R.; Radu, E. Kerr black holes with scalar hair. *Phys. Rev. Lett.* **2014**, *112*, 221101. [CrossRef] [PubMed]
48. Lemos, J.P.; Zanchin, V.T. Regular black holes: Electrically charged solutions, Reissner-Nordström outside a de Sitter core. *Phys. Rev. D* **2011**, *83*, 124005. [CrossRef]
49. Soroushfar, S.; Saffari, R.; Kamvar, N. Thermodynamic geometry of black holes in f(R) gravity. *Eur. Phys. J. C* **2016**, *76*, 476. [CrossRef]
50. Hendi, S.H.; Li, G.Q.; Mo, J.X.; Panahiyan, S.; Panah, B.E. New perspective for black hole thermodynamics in Gauss–Bonnet–Born–Infeld massive gravity. *Eur. Phys. J. C* **2016**, *76*, 571. [CrossRef]

51. Mo, J.X.; Li, G.Q.; Xu, X.B. Combined effects of f (R) gravity and conformally invariant Maxwell field on the extended phase space thermodynamics of higher-dimensional black holes. *Eur. Phys. J. C* **2016**, *76*, 545. [CrossRef]
52. Cai, R.G.; Cao, L.M.; Li, L.; Yang, R.Q. PV criticality in the extended phase space of Gauss-Bonnet black holes in AdS space. *J. High Energy Phys.* **2013**, *2013*, 5. [CrossRef]
53. Cai, R.G.; Hu, Y.P.; Pan, Q.Y.; Zhang, Y.L. Thermodynamics of black holes in massive gravity. *Phys. Rev. D* **2015**, *91*, 024032. [CrossRef]
54. Azreg-Ainou, M. Black hole thermodynamics: No inconsistency via the inclusion of the missing P–V terms. *Phys Rev. D* **2015**, *91*, 064049. [CrossRef]
55. Sadeghi, J.; Pourhassan, B.; Rostami, M. P–V criticality of logarithm-corrected dyonic charged AdS black holes. *Phys. Rev. D* **2016**, *94*, 064006. [CrossRef]
56. Hendi, S.H.; Momennia, M. AdS charged black holes in Einstein–Yang–Mills gravity's rainbow: Thermal stability and P–V criticality. *Phys. Lett. B* **2018**, *777*, 222–234. [CrossRef]
57. Aman, J.E.; Pidokrajt, N. Geometry of higher-dimensional black hole thermodynamics. *Phys. Rev. D* **2006**, *73*, 024017. [CrossRef]
58. Johnston, D.; Janke, W.; Kenna, R. Information geometry, one, two, three (and four). *arXiv* **2003**, arXiv:cond-mat/0308316.
59. Nulton, J.D.; Salamon, P. Geometry of the ideal gas. *Phys. Rev. A* **1985**, *31*, 2520. [CrossRef]
60. Ferrara, S.; Kallosh, R.; Strominger, A. N = 2 extremal black holes. *Phys. Rev. D* **1995**, *52*, R5412. [CrossRef]
61. Mahmoudi, S.; Jafarzade, K.; Hendi, S.H. A comprehensive review of geometrical thermodynamics: From fluctuations to black holes. *Turk. J. Phys.* **2023**, *47*, 214–278. [CrossRef]
62. Oshima, H.; Obata, T.; Hara, H. Differential-Geometry of Discrete Stochastic Processes. *J. Korean Phys. Soc.* **1998**, *32*, 773–785.
63. Ruppeiner, G. Thermodynamics: A Riemannian geometric model. *Phys. Rev. A.* **1979**, *20*, 1608–1613. [CrossRef]
64. Minamitsuji, M. Solutions in the scalar-tensor theory with nonminimal derivative coupling. *Phys. Rev. D* **2014**, *89*, 064017. [CrossRef]
65. Broderick, A.E.; Johannsen, T.; Loeb, A.; Psaltis, D. Modeling seven years of event horizon telescope observations with radiatively inefficient accretion flow models. *Astrophys. J.* **2016**, *820*, 137. [CrossRef]